Atmos. Chem. Phys., 16, 7725–7741, 2016
www.atmos-chem-phys.net/16/7725/2016/
doi:10.5194/acp-16-7725-2016

Atmospheric Chemistry and Physics Open Access EGU

Understanding isoprene photooxidation using observations and modeling over a subtropical forest in the southeastern US

Luping Su[1], Edward G. Patton[2], Jordi Vilà-Guerau de Arellano[3], Alex B. Guenther[4], Lisa Kaser[5], Bin Yuan[6,7], Fulizi Xiong[8], Paul B. Shepson[8,9], Li Zhang[10], David O. Miller[10], William H. Brune[10], Karsten Baumann[11], Eric Edgerton[11], Andrew Weinheimer[5], Pawel K. Misztal[12], Jeong-Hoo Park[13], Allen H. Goldstein[12,14], Kate M. Skog[15], Frank N. Keutsch[16,17], and John E. Mak[1]

[1]School of Marine and Atmospheric Sciences, Stony Brook University, Stony Brook, NY, USA
[2]Mesoscale and Microscale Meteorology Laboratory, National Center for Atmospheric Research, Boulder, CO, USA
[3]Meteorology and Air Quality Section, Wageningen University and Research Centre, Wageningen, the Netherlands
[4]Department of Earth System Science, University of California, Irvine, CA, USA
[5]Atmospheric Chemistry Observations & Modeling Laboratory, National Center for Atmospheric Research, Boulder, CO, USA
[6]Earth System Research Laboratory, Chemical Sciences Division, National Oceanic and Atmospheric Administration, Boulder, CO, USA
[7]Cooperative Institute for Research in Environmental Sciences, University of Colorado, Boulder, CO, USA
[8]Department of Chemistry, Purdue University, West Lafayette, IN, USA
[9]Department of Earth, Atmospheric and Planetary Sciences, Purdue University, West Lafayette, IN, USA
[10]Department of Meteorology, Pennsylvania State University, University Park, PA, USA
[11]Atmospheric Research and Analysis Inc., Cary, NC, USA
[12]Department of Environmental Science, Policy, & Management, University of California at Berkeley, Berkeley, CA, USA
[13]Climate and Air Quality Research Department, National Institute of Environmental Research, Incheon, Republic of Korea
[14]Department of Civil and Environmental Engineering, University of California at Berkeley, Berkeley, CA, USA
[15]Department of Chemistry, University of Wisconsin, Madison, WI, USA
[16]School of Engineering and Applied Sciences, Harvard University, Cambridge, MA, USA
[17]Department of Chemistry and Chemical Biology, Harvard University, Cambridge, MA, USA

Correspondence to: John E. Mak (john.mak@stonybrook.edu)

Received: 13 October 2015 – Published in Atmos. Chem. Phys. Discuss.: 11 November 2015
Revised: 19 May 2016 – Accepted: 8 June 2016 – Published: 24 June 2016

Abstract. The emission, dispersion, and photochemistry of isoprene (C_5H_8) and related chemical species in the convective boundary layer (CBL) during sunlit daytime were studied over a mixed forest in the southeastern United States by combining ground-based and aircraft observations. Fluxes of isoprene and monoterpenes were quantified at the top of the forest canopy using a high-resolution proton transfer reaction time-of-flight mass spectrometer (PTR-TOF-MS). Snapshot (∼ 2 min sampling duration) vertical profiles of isoprene, methyl vinyl ketone (MVK) + methacrolein (MACR), and monoterpenes were collected from aircraft every hour in the CBL (100–1000 m). Both ground-based and airborne collected volatile organic compound (VOC) data are used to constrain the initial conditions of a mixed-layer chemistry model (MXLCH), which is applied to examine the chemical evolution of the O_3–NO_x–HO_x–VOC system and how it is affected by boundary layer dynamics in the CBL. The chemical loss rate of isoprene (∼ 1 h) is similar to the turbulent mixing timescale (0.1–0.5 h), which indicates that isoprene concentrations are equally dependent on both photooxidation and boundary layer dynamics. Analysis of a model-derived concentration budget suggests that diurnal evolution of isoprene inside the CBL is mainly controlled by surface emissions and chemical loss; the diurnal evolution

of O_3 is dominated by entrainment. The NO to HO_2 ratio ($NO : HO_2$) is used as an indicator of anthropogenic impact on the CBL chemical composition and spans a wide range (1–163). The fate of hydroxyl-substituted isoprene peroxyl radical ($HOC_5H_8OO^\bullet$; ISOPOO) is strongly affected by $NO : HO_2$, shifting from NO-dominant to NO–HO_2-balanced conditions from early morning to noontime. This chemical regime change is reflected in the diurnal evolution of isoprene hydroxynitrates (ISOPN) and isoprene hydroxy hydroperoxides (ISOPOOH).

1 Introduction

Isoprene (C_5H_8) from biogenic emissions is the most abundant non-methane volatile organic compound (VOC) in the atmosphere (Guenther et al., 1995). Once emitted, the distribution of isoprene within the convective CBL is controlled via both photochemical oxidation and turbulent mixing. VOC emissions from forests have been studied extensively for more than 20 years (Guenther et al., 1991). More recent work has expanded the focus from emissions to impacts on regional forest chemistry (Kim et al., 2010; Karl et al., 2013; Park et al., 2013). These advances have exposed large uncertainties and unknown mechanisms in both chemistry and dynamics.

Isoprene chemistry over tropical forests has also been studied due to its influence on tropospheric chemistry through high emission (Karl et al., 2007) and proposed impact on OH recycling mechanisms under low-NO_x conditions ($NO_x \equiv NO + NO_2$) (Lelieveld et al., 2008; Whalley et al., 2011). Isoprene oxidation is usually initiated by addition of an OH to one of the C=C double bonds followed by fast reaction with O_2. Eight isomeric hydroxyl-substituted isoprene peroxyl radicals ($HOC_5H_8OO^\bullet$; ISOPOO) are then produced (Orlando and Tyndall, 2012). Large uncertainties arise in the subsequent reactions of ISOPOO radicals. In pristine tropical forest areas, the HO_2 pathway likely dominates (Paulot et al., 2009). Other reactions include self- and cross-reactions with organic peroxyl radicals (RO_2) and unimolecular isomerization (Peeters and Muller, 2010; Crounse et al., 2011).

Under NO-dominant conditions, ISOPOO mainly reacts with NO to produce NO_2, methyl vinyl ketone (MVK), and methacrolein (MACR). In urban environments where anthropogenic emissions of NO_x and non-methane hydrocarbons (NMHCs) are high, model outputs generally agree with observations of OH concentration during noontime (Shirley et al., 2006). However, for urban environments where NO_x mixing ratios vary by several orders of magnitude, model simulation outputs still underestimate the observed OH under low NO mixing ratios (< 1 ppbv) (Hofzumahaus et al., 2009; Lu et al., 2012). As a result, additional information on $HO_2 \rightarrow$ OH recycling process is needed to bridge the gap between model outputs and observations.

While large efforts have been dedicated to the study of reactive VOC chemistry, the temporal and spatial variation in those species in the convective CBL is also affected by the boundary layer dynamics (Kristensen et al., 2010). Regional model simulations are carried out to study the interplay between chemistry and dynamics. Depending on the complexity levels of dynamics representation, models can range from the simple zero-dimensional box model without accounting for the fluid dynamics (van Stratum et al., 2012) to mixed-layer model (extending zero-dimensional model by including the main dynamic processes of the CBL) (de Arellano et al., 2011) to one-dimensional transport model (Gao et al., 1993; Kristensen et al., 2010) to complex large eddy simulation (LES) (Patton et al., 2001). Box models are easy to implement but they are unable to incorporate the influence of the dynamical processes controlling the atmospheric boundary layer's diurnal evolution. LES resolves the turbulence and associated organized structures, but is computationally expensive, especially when coupled with complex chemical schemes. The mixed-layer model represents a useful compromise between a box model and an LES; it is suitable for studying both the boundary layer dynamics and the O_3–NO_x–HO_x–VOC chemistry within the measurement scale of this study while still maintaining the simplicity of a zero-dimensional model ($HO_x \equiv HO_2 + OH$) (de Arellano et al., 2011).

The Southeast Atmosphere Study (SAS) campaign was carried out during summer 2013 in Alabama. The campaign included comprehensive observations of VOCs and other trace gases (e.g., O_3, NO_x, and HO_x) from airborne and ground-based platforms (Hidy et al., 2014). In this study, we investigated the photochemistry of isoprene based on both ground-based and airborne observations during the SAS campaign. The experiment layout is shown in Fig. 1, which also includes a schematic of the important processes controlling the diurnal evolution of chemical species in the boundary layer. During the campaign, vertical profiles of VOCs were quantified with airborne sampling and subsequent measurements by using a proton transfer reaction time-of-flight mass spectrometer (PTR-TOF-MS). Ground-based eddy covariance (EC) was used to measure VOC fluxes on a tower above the forest canopy. A mixed-layer chemistry model was used to study how different processes (entrainment, boundary layer dynamics, surface emission, deposition, chemical production and loss) control the evolution of trace gases inside the CBL. SAS observations are used to impose the early morning initial conditions and the surface/free-tropospheric boundary conditions. We discuss isoprene photochemistry by focusing on the fate of ISOPOO radicals under different $NO : HO_2$ values.

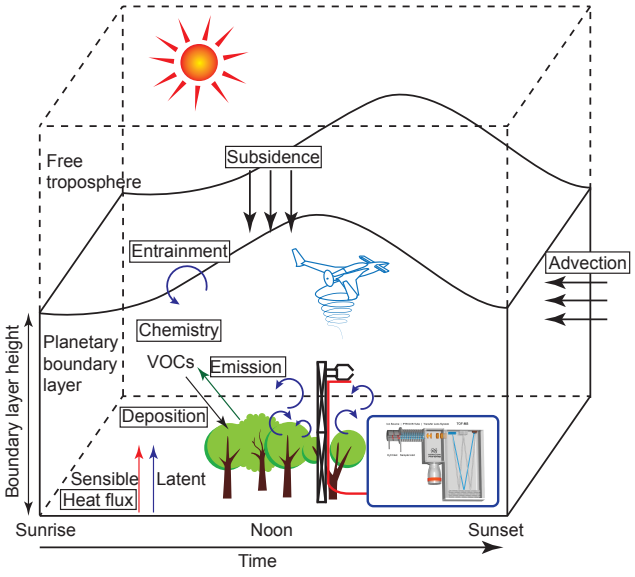

Figure 1. Schematic of the observations and various processes simulated in the mixed-layer model in this study.

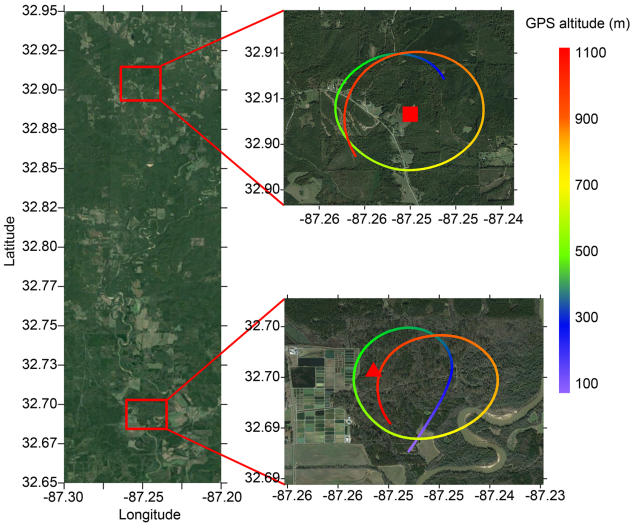

Figure 2. Location of the two ground-based sampling sites and typical flight tracks of Long-EZ aircraft. The left panel shows the locations of the SEARCH site (upper red rectangular area) and the AABC site (lower red rectangular area). The two panels on the right side show the typical flight tracks carried out on 12 June over the two sites. The solid red square and solid red triangle indicate the location of the sampling towers at the SEARCH site and the AABC site, respectively. The GPS altitude of both flight tracks are color-coded and indicated by the legend on the right. The maps were obtained from Google Earth.

2 Experimental

2.1 Field sites

The SAS field campaign was carried out during the summer of 2013 (from 1 June to 15 July) in central Alabama. There were two ground-based sampling sites: one near Marion, AL, at the Alabama Aquatic Biodiversity Center (32°41′40″ N, 87°14′55″ W; hereafter referred to as the AABC site), and the other one was located near Centreville, AL, which is part of the South-Eastern Aerosol Research and Characterization network (32°54′12″ N, 87°15′0″ W; hereafter referred to as the SEARCH site), situated about 24 km to the north-northwest of the AABC site (Fig. 2). The two sampling sites were located inside mixed forest canopies. The tower-based observations described in this paper are focused on the AABC site, where the average canopy height was ∼ 35 m. Eight 100 m step transects conducted in the footprint of the AABC flux tower showed that the forest was composed of 26 % *Liquidambar styracilfua* (sweetgum), 21 % *Nyssa* sp. (tupelos), 16 % *Pinus* sp. (pines), 14 % *Quercus* sp. (oaks), 11 % *Liriodendron* sp. (tulip poplars), 9 % *Taxodium* sp. (baldcypress), and 3 % *Ostrya* sp. (hophornbeams).

2.2 Air sample collection

Two sets of sampling systems were implemented simultaneously during the SAS campaign. Vertical profiles of air above the forest canopy and inside the CBL (100–1000 m above mean sea level (m a.s.l.)) were collected by using the Whole Air Sample Profiler (WASP) system installed on a model Long-EZ research airplane (Mak et al., 2013). The WASP system is integrated with a meteorological data monitoring system (the Aircraft-Integrated Meteorological Measurement System (AIMMS-20), Aventech Research Inc.), which was used to measure the ambient temperature, relative humidity (RH), GPS altitude, latitude, longitude, and 3-D wind components. In brief, the WASP system includes a 150 m coiled tubing, which is used to collect the ambient air sample during the aircraft's ascending phase. The altitude of the air samples collected inside the tubing is "marked" by injecting tracer gas (propene, C_3H_6) into the air stream at a preset frequency. For detailed description of the principle of the WASP system refer to Sect. 4.2 and (Mak et al., 2013). Flights were carried out during the day (10:00–17:00 Central Standard Time (CST)), when intensive photooxidation and turbulent mixing occurred. The time interval for sample collection was ∼2 min (Table 1). The aircraft usually started sampling from ∼ 100 m above the ground level and stopped at ∼ 1000 m (see Sect. 5). After each research flight (RF), the WASP tubing was sealed and transported to the AABC site in ∼ 30 min, where the air samples inside the tubing were analyzed by a high-resolution proton transfer reaction time-of-flight mass spectrometer (PTR-TOF-MS 8000, Ionicon Analytik GmbH, Austria). A total of 14 RFs were carried out (five over the SEARCH site and nine over the AABC site; Table 1) between 1 and 13 June 2013.

Table 1. Summary of the WASP research flights (RFs). The first four digits in "RF no." before the underscore indicate the month and day of the flight, while the digit after the underscore indicates the flight number carried out on the specific single day.

RF no.	Site	Latitude (°)	Longitude (°)	Sampling time (CST)	Temperature (°C)	RH
0601_2	AABC	32.69 to 32.71	−87.26 to −87.24	06:55–06:57	18.9–22.2	0.8–0.9
0605_1	SEARCH	32.90 to 32.91	−87.26 to −87.24	10:05–10:07	21.2–26.2	0.7–0.9
0605_4	AABC	32.69 to 32.71	−87.26 to −87.23	14:23–14:25	22.6–28.2	0.6–0.7
0606_1	SEARCH	32.90 to 32.91	−87.26 to −87.24	10:47–10:49	19.1–24.1	0.7–0.8
0606_3	AABC	32.69 to 32.70	−87.25 to −87.24	14:17–14:19	21.7–25.7	0.7–0.8
0606_5	AABC	32.69 to 32.71	−87.26 to −87.24	16:06–16:09	21.5–27.2	0.7–0.8
0608_3	AABC	32.69 to 32.71	−87.26 to −87.23	12:42–12:44	20.3–25.8	0.6–0.8
0611_1	SEARCH	32.90 to 32.91	−87.26 to −87.24	10:06–10:08	22.6–27.8	0.6–0.8
0611_3	AABC	32.69 to 32.70	−87.25 to −87.24	12:34–12:36	23.2–29.1	0.6–0.7
0611_5	AABC	32.69 to 32.70	−87.25 to −87.23	16:09–16:11	24.2–31.1	0.5–0.7
0612_1	SEARCH	32.90 to 32.91	−87.26 to −87.24	09:51–09:53	22.2–28.5	0.7–0.8
0612_4	SEARCH	32.90 to 32.91	−87.26 to −87.24	15:01–15:03	25.1–31.0	0.5–0.6
0613_2	AABC	32.69 to 32.70	−87.25 to −87.23	11:23–11:25	23.2–29.8	0.6–0.7
0613_4	AABC	32.68 to 32.70	−87.25 to −87.22	14:13–14:15	24.3–31.0	0.5–0.7

VOC eddy covariance (EC) fluxes were measured from the top of the forest canopy at the AABC site between 1 June and 14 July 2013 using the same PTR-TOF-MS. A 3/8 in. outer diameter (OD) perfluoro alkoxy (PFA) tubing (~ 50 m length, not heated) was mounted from the top of the flux tower (44 m) to the field laboratory trailer on the ground level. Sample air flow was $\sim 30\,\mathrm{L\,min^{-1}}$, an aliquot of which was diverted to the PTR-TOF-MS.

2.3 Instrumentation

The PTR-TOF-MS was used for two different measurement purposes during the SAS campaign: (1) quantification of the vertical profiles of speciated VOC mixing ratios above the ground-based sites by measuring air samples collected from the WASP system and (2) measurements of air samples through the EC inlet on top of the AABC flux tower, which are used for subsequent calculation of VOC fluxes. The two measurements overlapped between 1 and 13 June. For the overlapping period, an average of four WASP samples were measured each day and each sample took ~ 15 min to analyze. During the gap between two WASP sampling periods, the PTR-TOF-MS was connected to the EC line.

The basic principle of PTR-TOF-MS is described in Jordan et al. (2009) and Graus et al. (2010). During the campaign, the PTR-TOF-MS was operated in H_3O^+ mode, which uses hydronium ions (H_3O^+) as the primary reagent ions to ionize VOC species. The ionization conditions in the drift tube were controlled by setting the drift voltage to 575 V, drift temperature to 70 °C and drift pressure to 2.3 mbar, resulting in an E/N value of about 120 Td (with E being the electric field strength and N the gas number density; $1\,\mathrm{Td} = 10^{-17}\,\mathrm{V\,cm^2}$). The integration time was set to 1 and 0.1 s for WASP and EC measurements, respectively. A 1/16 in. OD capillary PEEK inlet (~ 1 m length) heated to 70 °C was used as a transfer line. For analyses of the WASP samples, the flow rate was set at 500 standard cubic centimeters per minute (sccm). The transfer line was connected to an unheated 1/8 in. OD PFA tubing (1 m length), which was connected to the WASP system outlet. For EC samples, the transfer line was connected to the EC line through an unheated 1/8 in. OD PFA tubing (10 cm length). Standard gas calibrations were performed daily by using a custom-built dynamic dilution system. Zero air was produced by pumping ambient air outside of the trailer through a catalytic convertor heated to 400 °C (platinum on quartz wool, Shimadzu Scientific Instrument Inc.). Gravimetrically prepared standard gas (Apel & Reimer) was dynamically diluted by the zero air and analyzed using the PTR-TOF-MS. Diiodomethane (CH_2I_2, Sigma-Aldrich, USA) was added as an external mass scale calibration source (shown as a fragment CH_2I^+ at exact $m/z = 140.920$ in the spectrum) through headspace permeation. Diiodomethane was stored inside a 1/4 in. OD glass tubing (~ 5 cm length) with one end melted and sealed. The other end of the glass tubing was connected to the PTR-TOF-MS sampling inlet through a 1/16 in. OD capillary PEEK tubing (~ 2 cm length) and a reducing union.

2.4 Other measurements

A suite of additional observations were used to constrain the initial and boundary conditions of the MXLCH model. Airborne measurements of isoprene, MVK+MACR, monoterpenes, other trace gases (O_3, NO_x), photolysis rates, and meteorological data (potential temperature and relative humidity) were collected on 12 June 2013 using the NCAR C-130 aircraft. Ground-based observations from the SEARCH site include trace-gas concentrations (O_3, NO_x, HO_x, HCHO) and boundary layer height measurements. Three-dimensional wind components (at 20 Hz) measured

at the top of the AABC flux tower were used for eddy covariance calculations. A list of the observed parameters and the corresponding measurement methods and uncertainties is summarized in Table S1 in the Supplement.

3 Data processing

3.1 PTR-TOF-MS data processing

The PTR-TOF-MS is capable of recording a full mass scan range (1–300 m/z in this study) with high mass resolution and time resolution while still maintaining sufficient sensitivity. However, such a setup can produce data files of a significant size. For processing the data generated by the PTR-TOF-MS, we developed a customized toolbox (Time-of-Flight INterpreting moDule, ToFIND), which is implemented in MATLAB (R2013b, MathWorks Inc., USA). The main routine consists of four subroutines (see Supplement Sect. S1 for detailed descriptions):

a. Peak shape fitting: the signals generated by the PTR-TOF-MS are featured with asymmetric peak shape. A fast fitting algorithm optimized for this application is implemented and used by the following three subroutines.

b. Time-of-flight to m/z conversion: parameters are calculated for each cycle to convert the time of flight to corresponding m/z.

c. Peak detection: the high mass-resolving power of PTR-TOF-MS enables detection of multiple peaks coexisting in one nominal m/z. A peak detection algorithm is implemented to automatically find those coexisting peaks.

d. Signal integration: the left and right bounds for each peak are defined and the signals within the two bounds are summed.

The data output from the ToFIND toolbox (in units of counts per second (cps)) is then normalized and corrected for duty cycle (resulting in units of normalized cps (ncps)) (Cappellin et al., 2012). The sensitivities for the target VOCs are calculated by using the standard gas calibration system as described above (see Sect. 2.3). The sensitivities (mean $\pm$ 1 standard deviation) during the whole campaign period for isoprene, MVK+MACR, and monoterpenes are 8.27 ± 0.28, 13.63 ± 1.44, and 9.22 ± 0.91 ncps ppbv^{-1}, respectively (see Fig. S7 in the Supplement). The instrumental uncertainties for these three VOCs are estimated to be 20 % during this campaign.

3.2 WASP data processing

WASP samples were analyzed by using the PTR-TOF-MS system and the mixing ratios of target VOC species were calculated by using the method described above. The dataset for each RF contains the mixing ratios of the VOC species aligned with the concurrent raw signal intensities of the tracer gas (C_3H_6, propene) (Mak et al., 2013). The injection pulses of the tracer gas were recorded separately and integrated into the AIMMS-20 output data. In order to reconstruct the altitude of the VOC mixing ratios, the injection pulse signals were aligned with the corresponding propene peak centers. The time resolution of the GPS altitude data and injection pulses is 0.2 and 10 s, respectively. As a result there are 50 GPS altitude data points within two adjacent injection pulses. The time resolution for the VOC data measured by the PTR-TOF-MS is constant at 1 s. However, the number of VOC data points between two tracer gas peaks is determined by a few factors, including the PTR-TOF-MS inlet flow rate (500 sccm), the difference of tubing inner diameters (ID) between the PTR-TOF-MS inlet and the WASP coiled tube, and the diffusion of the tracer gas inside the WASP coiled tube during the transportation time period. Thus the number of VOC data points between two tracer gas peaks is not constant (usually between 42 and 48). To resolve this problem, the GPS altitude data between two adjacent injection pulses were interpolated to generate the same number of data points as the VOC data between two propene peak centers. Then each VOC data point was assigned a corresponding GPS altitude, and the updated dataset for each RF contains the mixing ratios of the VOC species aligned with the corresponding GPS altitude.

4 Mixed-layer chemistry model

In this study we focus on the convective atmospheric boundary layer observed during the daytime. The vertical profiles of potential temperature and specific humidity (Fig. S1) show that the CBL was characterized by well-mixed profiles of these observed dynamic variables. It is therefore reasonable to employ mixed-layer theory to predict the boundary layer's dynamical evolution and most importantly the boundary layer height. The mixed-layer model we use is called MXLCH; MXLCH is a zero-dimensional spatial model which is described in detail elsewhere (de Arellano et al., 2011; van Stratum et al., 2012; de Arellano et al., 2015). The source code of MXLCH can be accessed at https://github.com/classmodel/mxlch (Vilà-Guerau de Arellano, 2016). In brief, MXLCH is based on the following assumptions:

1. In daytime CBL, the quantities (e.g., potential temperature, specific humidity, trace-gas mixing ratios) are perfectly mixed due to strong turbulent mixing and there is only one bulk value for each quantity throughout the CBL. In addition, the CBL growth depends on the conditions at the entrainment zone and at the free troposphere (FT).

Table 2. The initial and boundary conditions used in MXLCH.

Parameter	Symbol	Value	Units
Initial BL height	h	500[a]	m
Subsidence rate	w	9.0×10^{-6}	s^{-1}
Surface sensible heat flux	$\overline{w'\theta'_s}$	$0.10 \sin(\pi t/t_d)$[b]	$K\,m\,s^{-1}$
Surface latent heat flux	$\overline{w'q'_s}$	$0.15 \sin(\pi t/t_d)$[b]	$g\,kg^{-1}\,m\,s^{-1}$
Entrainment/surface heat flux ratio	$\beta = -\overline{w'\theta'_e}/\overline{w'\theta'_s}$	0.2	1
Initial BL potential temperature	$\langle\theta\rangle$	296.6[c]	K
Initial FT potential temperature	θ_{FT}	298.1	K
Potential temperature lapse rate FT	γ_θ	0.003	$K\,m^{-1}$
Advection of potential temperature	A_θ	6.40×10^{-4}	$K\,s^{-1}$
Initial BL specific humidity	$\langle q\rangle$	16.8[c]	$g\,kg^{-1}$
Initial FT specific humidity	q_{FT}	12.8	$g\,kg^{-1}$
Specific humidity lapse rate FT	γ_q	-0.004	$g\,kg^{-1}\,m^{-1}$
Advection of specific humidity	A_q	1.50×10^{-4}	$g\,kg^{-1}\,s^{-1}$

[a] Data from ceilometer measurement at the SEARCH site. [b] The peak values of the heat fluxes are obtained from the AABC tower. t is the elapsed time since the start of the simulation and t_d is the time difference between the start and end of the simulation period (06:00–16:30 CST). [c] Data from the AABC flux tower.

2. The CBL height growth is driven by the surface sensible heat and latent heat fluxes. These two variables were prescribed in the model based on observations.

3. The CBL and the FT are separated by an infinitesimally thin inversion layer. Through this layer there is an entrainment flux that exchanges state variables and reactants following the CBL dynamics.

4. Large-scale meteorological forcings (e.g., subsidence, and advection of heat and moisture) are prescribed to the model as external forcings.

5. MXLCH neglects species segregation that could modify chemical reaction rates (Ouwersloot et al., 2011).

In what follows, we use MXLCH to model the evolution of the CBL and trace-gas chemistry during SAS toward further understanding of the processes controlling photochemistry inside the CBL.

4.1 Boundary layer meteorology

The meteorological conditions in MXLCH are constrained by the available observations. To reduce the uncertainties introduced from daily variations, averaged values of the variables (both meteorological data and O_3–NO_x–HO_x concentrations) from selected days (5, 6, 8, 10–13 June) were calculated and used as the constraints of the initial boundary conditions in MXLCH (Table 2). The selected days were chosen based on (1) cloud coverage (indicated by photosynthetically active radiation (PAR)), (2) O_3 diurnal profiles, and (3) data availability. Averaged diurnal profiles for PAR and O_3 are obtained based on the data between 1 and 14 June 2013 (Fig. S2). Days with data deviate from the averaged values for more than 30 % in PAR or O_3 profiles are discarded. Days when WASP samples are not available are also neglected. The apparent sunrise and sunset occurred at 04:41 and 18:57 CST, respectively, during the study period (1 to 13 June 2013) (http://www.esrl.noaa.gov/gmd/grad/solcalc/). The averaged sensible and latent heat fluxes were significantly above zero during 06:00–16:30 and 06:00–18:00 CST (see Fig. S3), respectively. In this study, we focus on analyzing the processes under unstable CBL conditions driven primarily by the sensible heat flux. Hence, 06:00–16:30 CST is chosen as the model simulation time interval. During the studied time period, the wind directions at the AABC site were mainly from the southeast, with wind speed below $2\,m\,s^{-1}$ for most of the time (Fig. S4).

4.2 Biogenic volatile organic compound (BVOC) fluxes

Isoprene and monoterpenes were the two dominant VOC emissions observed at the top of the forest canopy. MXLCH simulations use imposed emissions of these two VOC species by the observed EC flux data at the AABC flux tower. The EC data from selected days (listed in Sect. 3.1) were averaged to produce a single diurnal flux evolution, where a sinusoidal function was fit to the observed VOC flux temporal evolution taking sampling time as the independent variable (see Fig. S5 and Table 3).

4.3 NO_x fluxes

The forest–atmosphere exchange of NO_x affects the oxidative capacity of the CBL through reactions involved in the O_3–NO_x–HO_x–VOC system. The study of forest–atmosphere NO_x exchange during daytime is challenging due to the fast conversion between NO and NO_2 within canopy in the presence of O_3. Direct measurements using

Table 3. The initial mixing ratios of important chemical species in the CBL and FT used in MXLCH.

Species	Mixing ratio in CBL (ppbv)	Mixing ratio in FT (ppbv)	Emission or deposition
O_3	12.9[a]	51.0[c]	2.3[d]
NO	0.1[a]	0.05[c]	[e]
NO_2	0.8[a]	0.06[c]	[f]
OH	0	0	–
HO_2	0	0	–
HCHO	2.0[a]	1.1[c]	–
C_5H_8	0.6[b]	0.0	$1.0\sin(\pi t/t_d)$[g]
MVK	0.3[b]	0.3[b]	2.4[d]
MACR	0.3[b]	0.3[b]	2.4[d]
ISOPND	0.01[a]	0	1.5[h]
ISOPNB	0.01[a]	0	1.5[h]
ISOPOOH	0	0	2.5[h]
Monoterpenes	1.1[b]	0.0	$0.070\sin(\pi t/t_d)$[g]

[a] Data are obtained from the SEARCH site. [b] Data are obtained from the WASP system. [c] Data are obtained from the NCAR C-130. [d] Dry deposition velocity (unit: $cm\,s^{-1}$); values taken from Karl et al. (2010).[e] $-5\sin(\pi t/t_d)$ $pptv\,m\,s^{-1}$ in reduced scheme; $-5\sin(\pi t/t_d)$, $-10\sin(\pi t/t_d)$, or $-30\sin(\pi t/t_d)$ $pptv\,m\,s^{-1}$ in complex scheme. t is the elapsed time since the start of the simulation and t_d is the time difference between the start and end of the flux period (06:00–08:00 CST). [f] $5\sin(\pi t/t_d)$ $pptv\,m\,s^{-1}$ in reduced scheme; $5\sin(\pi t/t_d)$, $10\sin(\pi t/t_d)$, or $30\sin(\pi t/t_d)$ $pptv\,m\,s^{-1}$ in complex scheme. t and t_d are the same as above. [g] The peak values of the BVOC fluxes are obtained from the AABC tower. t and t_d are the same as above. [h] Dry deposition velocity (unit: $cm\,s^{-1}$); values taken from Nguyen et al. (2015).

the eddy covariance technique at a site in the Sierra Nevada in California (June to July 2009) show a midday NO_x flux on the order of 1 to 20 $pptv\,m\,s^{-1}$, depending on meteorological conditions such as rain (Min et al., 2014). NO_x fluxes were downward during 06:00–09:00 and upward during 09:00–15:00 local time. NO_x eddy covariance fluxes reported in northern Michigan (July to August 2012) show mean NO and NO_2 flux peak values of -4.0 $pptv\,m\,s^{-1}$ (downward) and 4.8 $pptv\,m\,s^{-1}$ (upward), respectively (Geddes and Murphy, 2014).

NO_x eddy covariance flux observations are not available from during the SAS campaign. Using the soil temperature (at 4.4 cm depth) measured at the AABC flux tower, the soil NO flux (mean $\pm$ 1 standard deviation) is estimated to be 38.4 ± 5.0 $pptv\,m\,s^{-1}$ during the sampling period (1 to 13 June) following the parameterization of Thornton et al. (1997). This algorithm is based on pasture land cover type, and the calculated NO flux should be regarded as an upper bound since soil NO flux under forest land cover is lower (Thornton et al., 1997). In MXLCH, NO_x flux is prescribed with similar patterns as the observations listed above. NO has downward flux during early morning (06:00–08:00 CST), while NO_2 shows upward flux during 06:00–16:30 CST, with the same pattern as sensible heat flux. To assess the effect of different NO_x flux levels on the CBL photochemistry, we carry out sensitivity simulations with three different NO_x flux levels. In the base case, NO and NO_2 have minimum and maximum fluxes at -5 and 5 $pptv\,m\,s^{-1}$, respectively (denoted as $F_{NO_x} = \pm 5$ $pptv\,m\,s^{-1}$). The minimum or maximum flux value is used to produce a flux profile the same way as the BVOC flux described above. The other two NO_x flux levels are $F_{NO_x} = \pm 15$ and ± 30 $pptv\,m\,s^{-1}$. The sensitivity simulation results are discussed in Sect. 6.2.

4.4 Chemistry

Two chemistry schemes are coupled separately to MXLCH. In both chemical schemes, the general chemistry involving O_3–NO_x–HO_x system is obtained as a subset from the Model for Ozone and Related Chemical Tracers (MOZART, version 4) (Emmons et al., 2010). The first chemistry scheme is extended with a highly reduced version of MOZART chemical mechanism involving reactive VOC species (Table 4, hereafter referred to as the reduced scheme) (de Arellano et al., 2011). In the reduced scheme, (1) MVK and MACR are lumped together and considered as one compound, (2) no isoprene nitrate chemistry is implemented and the ISOPOO + NO channel recycles NO with 100 % yield of NO_2, (3) no isomerization channel is implemented for ISOPOO radicals, and (4) monoterpene oxidation products do not proceed to further reactions. The second chemistry scheme is extended with a subset from the GEOS-Chem v9-02 chemical scheme (Mao et al., 2013), which implements updated isoprene oxidation chemistry (Paulot et al., 2009; Peeters et al., 2009; Peeters and Muller, 2010; Crounse et al., 2011) (see Tables S2 and S3, hereafter referred to as the complex scheme). In the complex scheme, (1) the reaction rate of ISOPOO radicals through the HO_2 channel is updated to take into account of the size effect of the molecule; (2) the isomerization rate of ISOPOO radicals derived by Crounse et al. (2011) is used; (3) nighttime isoprene chemistry is not implemented in this study (this mainly involves reactions with NO_3

Table 4. The reduced chemistry scheme used in MXLCH. Product compounds shown in parentheses (e.g., (O_2)) indicate that these are not included in the model solution.

Number	Reaction	Reaction rate
R01	$O_3 + h\nu \rightarrow O(^1D) + (O_2)$	$3.03 \times 10^{-4} \exp(-1.96/cos(x))$
R02	$O(^1D) + H_2O \rightarrow 2OH$	$1.63 \times 10^{-10} \exp(60/T)$
R03	$O(^1D) + N_2 \rightarrow O_3$	$2.15 \times 10^{-11} \exp(110/T)$
R04	$O(^1D) + O_2 \rightarrow O_3$	$3.30 \times 10^{-11} \exp(55/T)$
R05	$NO_2 + h\nu \rightarrow NO + O_3$	$1.71 \times 10^{-2} \exp(-0.55/\cos(x))$
R06	$CH_2O + h\nu \rightarrow HO_2$	$1.94 \times 10^{-4} \exp(-0.82/\cos(x))$
R07	$OH + CO \rightarrow HO_2 + (CO_2)$	2.40×10^{-13}
R08	$OH + CH_4 \rightarrow CH_3O_2$	$2.45 \times 10^{-12} \exp(-1775/T)$
R09	$OH + C_5H_8 \rightarrow HOC_5H_8OO$	$3.10 \times 10^{-11} \exp(350/T)$
R10	$OH + [MVK + MACR] \rightarrow HO_2 + CH_2O$	2.40×10^{-11}
R11	$OH + HO_2 \rightarrow H_2O + (O_2)$	$4.80 \times 10^{-11} \exp(250/T)$
R12	$OH + H_2O_2 \rightarrow H_2O + HO_2$	$2.90 \times 10^{-12} \exp(-160/T)$
R13	$HO_2 + NO \rightarrow OH + NO_2$	$3.50 \times 10^{-12} \exp(250/T)$
R14	$CH_3O_2 + NO \rightarrow HO_2 + NO_2 + CH_2O$	$2.80 \times 10^{-12} \exp(300/T)$
R15	$HOC_5H_8OO + NO \rightarrow HO_2 + NO_2 + 0.7[MVK + MACR] + CH_2O$	1.00×10^{-11}
R16	$OH + CH_2O \rightarrow HO_2$	$5.50 \times 10^{-12} \exp(125/T)$
R17	$2HO_2 \rightarrow H_2O_2 + (O_2)$	[a]
R18	$CH_3O_2 + HO_2 \rightarrow$ product	$4.10 \times 10^{-13} \exp(750/T)$
R19	$HOC_5H_8OO + HO_2 \rightarrow 0.8OH +$ product	1.50×10^{-11}
R20	$OH + NO_2 \rightarrow HNO_3$	$3.50 \times 10^{-12} \exp(340/T)$
R21	$NO + O_3 \rightarrow NO_2 + (O_2)$	$3.00 \times 10^{-12} \exp(-1500/T)$
R22	$NO + NO_3 \rightarrow 2NO_2$	$1.80 \times 10^{-11} \exp(110/T)$
R23	$NO_2 + O_3 \rightarrow NO_3 + (O_2)$	[b]
R24	$NO_2 + NO_3 \rightarrow N_2O_5$	[c]
R25	$N_2O_5 \rightarrow NO_3 + NO_2$	$1.30 \times 10^{-2} \exp(-3.5/T)$
R26	$N_2O_5 + H_2O \rightarrow 2HNO_3$	2.50×10^{-22}
R27	$N_2O_5 + 2H_2O \rightarrow 2HNO_3 + H_2O$	1.80×10^{-39}
R28	$HO_2 + O_3 \rightarrow OH + 2(O_2)$	$2.03 \times 10^{-16} (T/300)^{4.57} \exp(693/T)$
R29	$C_{10}H_{16} + O_3 \rightarrow$ product	$5.00 \times 10^{-16} \exp(-530/T)$
R30	$C_{10}H_{16} + OH \rightarrow$ product	$1.21 \times 10^{-11} \exp(436/T)$
R31	$OH + O_3 \rightarrow HO_2 + (O_2)$	$1.30 \times 10^{-12} \exp(-956/T)$

[a] $k = (k_1 + k_2)/k_3$; $k_1 = 2.21 \times 10^{-13} \exp(600/T)$; $k_2 = 1.91 \times 10^{-33} \exp(980/T) c_{air}$; $k_3 = 1 + 1.4 \times 10^{-21} \exp(2200/T) c_{H_2O}$.
[b] $k = 0.35 \times (k_0 \times k_{inf})/(k_0 + k_{inf})$; $k_0 = 3.61 \times 10^{-30} (T/300)^{-4.1} c_{N_2}$; $k_{inf} = 1.91 \times 10^{-12} (T/300)^{0.2}$.
[c] $k = 0.35 \times (k_0 \times k_{inf})/(k_0 + k_{inf})$; $k_0 = 1.31 \times 10^{-3} (T/300)^{-3.5} \exp(-1100/T)$; $k_{inf} = 9.71 \times 10^{14} (T/300) \times \exp(-11\,080/T)$.

radicals); and (4) only the first-generation isoprene hydroxynitrates (ISOPN = β-hydroxy isoprene nitrate + δ-hydroxy isoprene nitrate) are discussed in this study. In the complex scheme, (3) and (4) are different from GEOS-Chem.

Photolysis rates in the complex scheme are calculated using the NCAR Tropospheric Ultraviolet and Visible (TUV) radiation model. The relationship between solar zenith angle (sza) and photolysis rates (j) is obtained by performing curve fitting to an empirical function $j = a \times \exp(b/\cos(\text{sza}))$, where a and b are two parameters obtained through curve fitting (Table S4 and Fig. S6). Aircraft observations of photolysis rates (from the NCAR C-130 aircraft) over the two ground sites are available during 14 June 2013 around noontime. The comparisons between TUV outputs and NCAR C-130 observations show that the differences between the two datasets with respect to the observations are within ±20 %, except for three reactions involving the photolysis of HNO_2, CH_3COCH_3, and $CH_3CO(OONO_2)$ (R09, R19, and R27, see Table S4), which range from ±47 to ±53 % (see Table S4).

5 Observation results

A summary of the spatial and temporal coverage for all RFs, together with the corresponding meteorological data, is shown in Table 1. Selected vertical profiles of isoprene, MVK + MACR, and monoterpenes are shown in Fig. 3. Recent laboratory experiments show that a significant fraction (44 %) of 1,2-ISOPOOH is converted to $C_4H_7O^+$ (same m/z as MVK+MACR) in PTR quadrupole MS (Rivera-Rios et al., 2014). To evaluate the interference

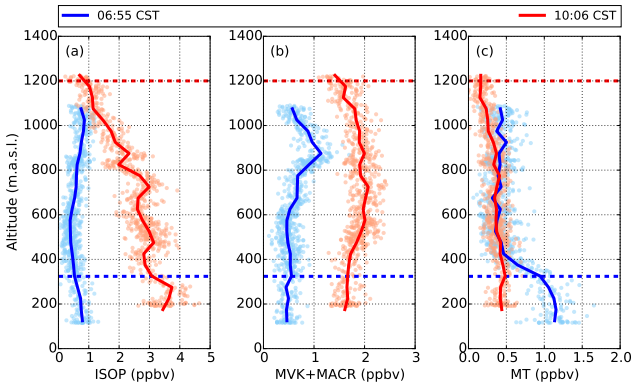

Figure 3. Vertical profiles of VOC species collected using the WASP system. Blue and red indicate data collected on 1 June 2013 (at 06:55 CST, over the AABC site) and on 11 June 2013 (at 10:06 CST, over the SEARCH site), respectively. The dots represent original data points from the WASP system. The solid lines represent averaged data from the corresponding original data points within each 50 m altitude intervals. The dashed lines represent the estimated boundary layer height from ceilometer measurements (see Fig. 4c). The y axis represents GPS altitude in units of meters above mean sea level (m a.s.l.). The elevation of the sampling sites is $\sim$ 67 m a.s.l.

of ISOPOOH on MVK+MACR, a laboratory experiment was carried out with the same PTR-TOF-MS used during the SAS campaign. The conversion rate of 1,2-ISOPOOH to $C_4H_7O^+$ is estimated to be 14^{+14}_{-6} % (see Supplement Sect. S2), which is lower than reported by Rivera-Rios et al. (2014). This indicates that the conversion rate may vary under different sampling setup and instrument configurations. It should be noted that the reported MVK+MACR mixing ratios measured with the WASP system are not corrected for the ISOPOOH interference due to the lack of concurrent ISOPOOH measurement. As a result, the uncertainty of MVK+MACR mixing ratios is estimated to be within 30 % when accounting for the ISOPOOH interference.

During the early morning (06:55 CST), the averaged mixing ratio of isoprene throughout the vertical profile was 0.60 ppbv, with slightly higher values towards the top and bottom of the profile. The low mixing ratio of isoprene above the canopy during this early time is caused by (1) a lack of solar radiation to fuel the biological production of isoprene, and (2) limited vertical turbulent mixing during the early morning hours due to stratification. The slightly higher isoprene in the residual layer at 1000 m might reflect the residual isoprene left from the previous day and preserved during the night due to the absence of photooxidation. The absence of photooxidation may also lead to the higher mixing ratios of MVK+MACR at 800–1000 m (Fig. 3b). The mixing ratios of monoterpenes within the nocturnal boundary layer ($>$ 1.00 ppbv) were significantly higher than in the residual layer ($\sim$ 0.30 ppbv) (Fig. 3c). These high monoterpene mixing ratios near the surface primarily result from nighttime emissions which are trapped within the shallow nocturnal boundary layer and lower chemical loss rates.

The vertical profiles of VOC species changed dramatically in air samples collected at 10:06 CST. The mixing ratios of isoprene developed a consistent gradient within the well-mixed CBL, with higher values right above the forest canopy and lower values near the top of the CBL. The mixing ratios of MVK+MACR were relatively uniform throughout the CBL. The different vertical profiles between isoprene and MVK+MACR result from their different chemical lifetime relative to the turbulent mixing timescales (see Sect. 6.2). The sharp gradient of monoterpenes near the top of the CBL (at 350 m) during early morning (Fig. 3c) is significantly reduced (0.50 ppbv near the ground and 0.20 ppbv near the CBL top) due to enhanced vertical turbulent mixing and increased OH concentration. It should be noted that the two different set of profiles were measured on different days and over different sampling sites (Fig. 3). Though we focus the discussion on sampling time during the day, other factors such as meteorology and sampling location could play important an part in the VOCs' vertical distribution.

One of the main goals of this study is to analyze different processes affecting the diurnal variation in the VOC species within the CBL. To achieve this, the boundary layer height (BLH) during each WASP RF was obtained from ground-based observations (Fig. 4c), and the mixing ratios within the BLH during the RF for each selected VOC species were averaged to produce a representative mixing ratio of this selected VOC species (Fig. 5g–i). Only one RF was carried out to investigate the VOC mixing ratios in early morning (at 06:55 CST). The rest of the RFs span over the convective daytime (10:00–16:00 CST). The evolution of VOC species inside the CBL in the context of surface emissions, other chemical species (e.g., O_3, NO_x, and HO_x), and boundary layer dynamics are discussed in detail in Sect. 6.2.

6 Model results and discussion

6.1 Boundary layer dynamics

MXLCH's ability to reproduce the boundary layer dynamics is essential for predicting the evolution of chemical species. The most important parameter is the BLH, which affects entrainment and turbulent mixing of chemical species inside the CBL. The model outputs of potential temperature, specific humidity, and BLH are shown in Fig. 4. The BLH growth is driven by sensible (H) and latent (LE) heat flux (parameterized based on observations; Fig. S3) and is regulated by subsidence and advection. The observations from the ceilometer and sounding system at the SEARCH site indicate a CBL growth rate of about 280 m h^{-1} during 07:00–10:00 CST and 80 m h^{-1} during 11:00–16:00 CST. A similar BLH growth rate is achieved with MXLCH (Fig. 4c) by adjusting the subsidence rate and the initial potential temperature difference

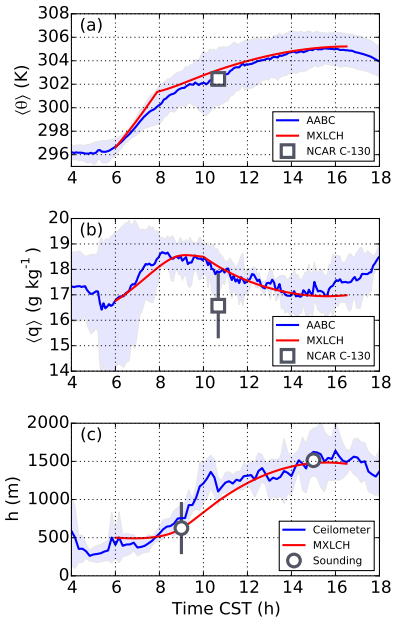

Figure 4. Diurnal evolution of **(a)** mixed-layer potential temperature ($\langle\theta\rangle$), **(b)** mixed-layer specific humidity ($\langle q\rangle$), and **(c)** boundary layer height (h). The solid blue lines indicate ground-based observations which are averaged over the low cloud cover days. The shaded areas and error bars indicate 1 standard deviation of the corresponding observations. The solid red lines indicate data from MXLCH outputs.

between the CBL and FT (Table 2). The BLH estimated from sounding data at 09:00 and 15:00 CST agree well with the model output (Fig. 4c). Due to the small potential temperature jump between the CBL and FT, the entrainment of relatively warmer air from the FT and surface heat flux is not sufficient to explain the evolution of potential temperature inside the CBL. Advection of relatively warm air is introduced into the system to match the MXLCH output with the observations on top of the AABC flux tower. The specific humidity starts to increase from the beginning of the model simulation due to the turbulent flux of humid air (Fig. S3), reaching a maximum value of 18.7 g kg^{-1} at 08:20 CST, and then gradually drops to 17.0 g kg^{-1} at around 15:00 CST; this diurnal variation results from the entrainment of relatively dry air from the FT into the CBL. The averaged potential temperature measured from the NCAR C-130 aircraft on 12 June agrees well with both ground-based observations and model outputs. The averaged specific humidity from the NCAR C-130 aircraft, with a large variability, is smaller than ground observations. In general, the MXLCH satisfactorily represents the boundary layer dynamics during the simulation time period of the day (06:00–16:30 CST), which gives us confidence to carry out further analyses of the two chemistry schemes.

6.2 Diurnal variation in chemical species

Comparisons between the two chemistry schemes together with the ground and airborne observations are shown in Fig. 5. It should be noted that ground-based observations (O_3, NO_x, HO_x, HCHO, ISOPN) are included in the comparison with the model bulk output in Fig. 5. This assumes the ground-based measurements are representative of the averaged concentrations inside the CBL, which may not apply for certain species with a short chemical lifetime (< 1 h). In the complex scheme sensitivity analyses, best agreement between observation and model output is achieved with $F_{NO_x} = \pm 30$ pptv m s^{-1} and ISOPN yield of 6 % (Fig. 5). In the discussion that follows, the complex scheme output refers to this best agreement configuration unless otherwise stated explicitly.

The diurnal evolution of the O_3–NO_x system from observations was divided into two phases. During 06:00–12:00 CST, NO_2 mixing ratios in the CBL showed a steep decrease at a rate of -100 pptv h^{-1}, which is mainly caused by photolysis. This is accompanied with a rapid increase in O_3 (3 ppbv h^{-1}). NO mixing ratios reached a peak value at 200 pptv during 06:00–08:00 CST and gradually decreased to 30 pptv after 12:00 CST. During 12:00–16:00 CST, O_3, NO, and NO_2 mixing ratios stayed relatively stable at 30 ppbv, 30 pptv, and 200 pptv, respectively. Airborne O_3 and NO_x mixing ratios (from NCAR C-130) were on the upper and lower bound of the ground-based observations, respectively. O_3 mixing ratios in both chemistry schemes fall within the uncertainty of the observations (Fig. 5a). O_3 mixing ratios in the reduced scheme are 5 ppbv higher than the complex scheme during 12:00–16:30 CST, which correlates to its higher NO_2 mixing ratios. NO mixing ratios in the reduced scheme are overestimated throughout the whole simulation time period (Fig. 5b). One possible cause is that isoprene nitrate chemistry is not implemented in the reduced scheme and the ISOPOO + NO pathway recycles NO with 100 % yield of NO_2, which maintains the elevated NO mixing ratios through photolysis during sunlit daytime. By implementing updated isoprene nitrate chemical mechanisms, the complex scheme agrees better with the observed NO mixing ratios (Fig. 5b). Applying the base NO_x flux ($F_{NO_x} = \pm 5$ pptv m s^{-1}) in the complex scheme will reduce the NO_x mixing ratios to below 80 pptv after 12:00 CST (Fig. S8), which is less than half of the observed NO_2 mixing ratio (200 pptv). The photochemical cascade will bring down the O_3 and OH radicals, leading to higher isoprene mixing ratios than observations during 10:00–16:00 CST (Fig. S8). Applying faster photolysis rates of second-generation isoprene nitrate products (methyl vinyl ketone nitrate (MVKN) 5.6×10^{-5} s^{-1} and methacrolein nitrate (MACRN) 3.5×10^{-4} s^{-1} as compared to 9.1×10^{-7} s^{-1} used for both compounds in the complex scheme) (Muller et al., 2014) does not bring up the NO_2 mixing ratio significantly (change is less than 5 %, data not shown). Thus, in the complex scheme

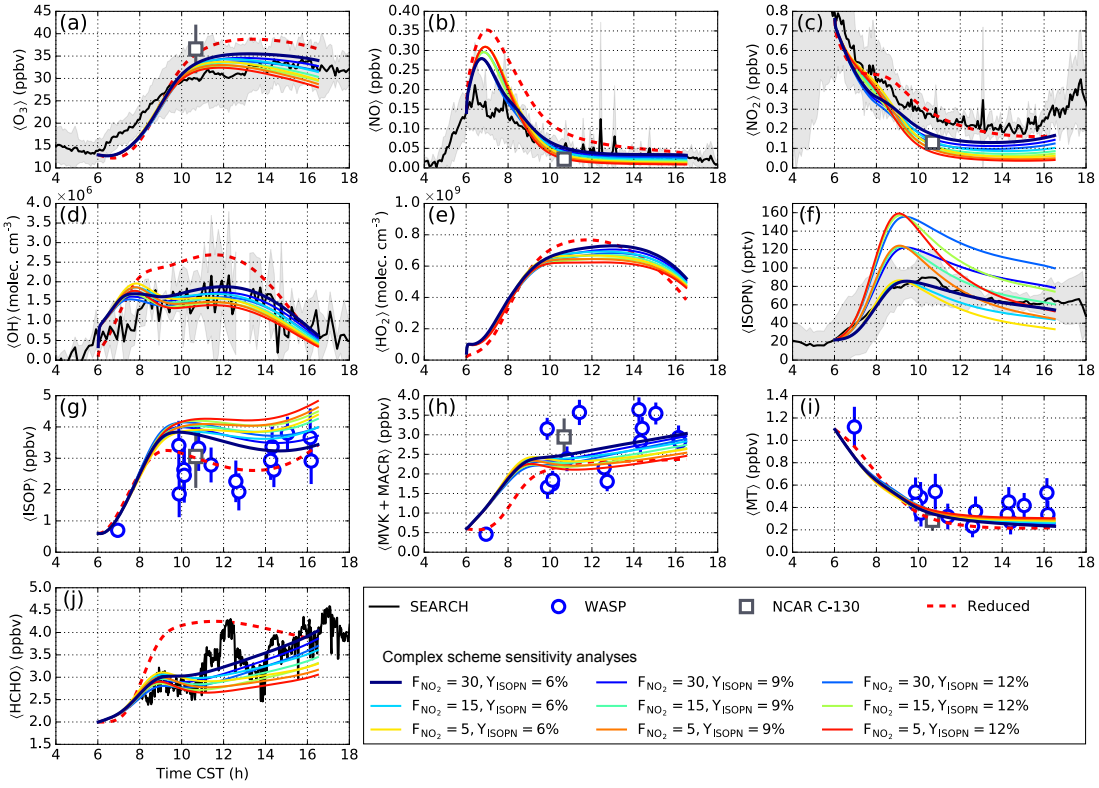

Figure 5. Diurnal variation in **(a)** O_3, **(b)** NO, **(c)** NO_2, **(d)** OH, **(e)** HO_2, **(f)** ISOPN, **(g)** isoprene, **(h)** MVK + MACR, **(i)** monoterpenes, and **(j)** HCHO. The solid black line and corresponding shaded light-gray area indicate the averaged value and 1 standard deviation from the observations at the SEARCH site. The solid blue circle and corresponding error bar indicate averaged value and 1 standard deviation of VOC mixing ratios within the boundary layer from each RF of the WASP system. The solid black square and corresponding error bar indicate averaged value and 1 standard deviation of chemical species within the boundary layer from RF of the NCAR C-130 aircraft. The solid black and red lines indicate the output from MXLCH model simulation with reduced and complex chemistry schemes, respectively. Data from the WASP system are from different days and RFs; see text for details.

higher NO_2 flux (30 pptv m s^{-1}) during noontime is necessary to maintain the NO_2 level in the presence of isoprene nitrate chemistry.

The reduced scheme overestimates OH radical concentration by 50 % during noontime, though it is still within the uncertainty of the observations. In the complex scheme, modeled OH radical concentrations generally agree well with the observations, except during the early morning (06:00–08:00 CST) when the model output is slightly higher than the observations (Fig. 5d). The higher OH radicals are mainly produced through the NO + HO_2 reaction, as fueled by the NO peak during the same time period. On the other hand, HO_2 radicals in the complex scheme are higher than those in the reduced scheme during 06:00–09:00 CST, which are mainly produced through RO_2 + NO pathways implemented in the complex scheme. Certain HO_2 loss processes that are not included in this study such as heterogeneous uptake onto aerosol particles (Whalley et al., 2010; Lu et al., 2012) may reduce the HO_2 concentration and subsequently OH radical concentration. HO_2 measurements during the selected study time period are not available due to instrument interference. HO_2 concentration measured on 25 June 2013 (with similar meteorological conditions as the selected days) is 1.0×10^9 molec. cm^{-3} during 12:00 CST, higher than both chemical scheme outputs (7.0×10^8 molec. cm^{-3}).

The mixing ratio of isoprene was less than 1.00 ppbv in the early morning (Fig. 5g). During sunlit daytime (10:00–16:00 CST), the mixing ratios of isoprene within the CBL varied between 1.50 and 4.00 ppbv, with lower mixing ratios during noontime (13:00 CST). This mirrored the higher mixing ratios of OH radicals during the same time period (Fig. 5d), indicating that the abundance of isoprene in the CBL is mainly controlled by photooxidation by OH radicals. MVK + MACR is the first-generation photooxidation product of isoprene, hence the mixing ratios of MVK + MACR loosely follow the mixing ratios of isoprene, with lower values during the early morning and similar mixing ratio range during daytime. The variation in isoprene within each WASP RF was larger than MVK + MACR during the daytime, which is reflected in the standard deviations. This is due to the relatively large gradient of isoprene vertical profiles (Fig. 3a). The large variability in isoprene vertical pro-

file can be attributed to its relatively short chemical lifetime during noontime (1 h), in contrast to MVK+MACR (10 h). The chemical lifetime of isoprene is closer to the turbulent mixing timescale (0.1–0.5 h). Another factor could be the land surface heterogeneity (see Fig. 2), which can cause large variability in isoprene vertical profiles through the effect of induced secondary circulations (Ouwersloot et al., 2011). The mixing ratios of monoterpenes showed higher values (1.10 ppbv) during the early morning (see Sect. 5), while during 10:00–16:00 CST, their mixing ratios fell between 0.20 and 0.60 ppbv with slightly lower values during noontime. VOC mixing ratios measured from the NCAR C-130 aircraft agree well with the WASP RF (Fig. 5g–i).

For the model outputs, the lowest isoprene concentration between 12:00 and 16:00 CST occurs at 14:00 CST in the complex scheme, which is 1 h later than that predicted by the reduced scheme and that observed (at 13:00 CST). One possible explanation to this difference is that the peak value of the OH radical concentrations in the complex scheme is delayed as compared with the reduced scheme during noontime. As for MVK + MACR, both chemical schemes produce results within the range of observations. Both schemes represent the lower bound of the observed monoterpenes during 10:00–16:00 CST. The mixing ratios of isoprene, MVK + MACR, and monoterpenes are lower in the reduced scheme, which is caused by its higher OH radical concentrations. The isoprene mixing ratio is most sensitive due to its high reactivity with OH radicals ($k_{C_5H_8+OH} = 1.0 \times 10^{-10}$ cm^3 molec.$^{-1}$ s^{-1}).

The mixing ratios of observed ISOPN show a peak value of 90 pptv at 10:00 CST and then gradually decreased to 60 pptv at 14:00 CST and remained relatively stable during 14:00–16:00 CST. The model outputs of ISOPN from the complex scheme generally agree with the observed data. The ISOPN yield in the complex scheme is set at 6 %, which is within the range of the results from the chamber experiments (9^{+4}_{-3} %) carried out at the SEARCH site (Xiong et al., 2015). Sensitivity simulations on two other different ISOPN yields at 9 and 12 % overestimate the ISOPN mixing ratios by 30 and 70 %, respectively, at 10:00 CST (Fig. 5f). Applying updated ozonolysis rate for δ-ISOPN (2.8×10^{-17} cm^{-3} molec.$^{-1}$ s^{-1}) and β-ISOPN (3.8×10^{-19} cm^{-3} molec.$^{-1}$ s^{-1}) (Lee et al., 2014) will cause the model to overestimate ISOPN concentration by 27–56 % during 12:00–16:00 CST with ISOPN yield of 6 % and F_{NO_x} = ±30 pptv m s^{-1}. The loss paths of ISOPN formed inside the CBL include photolysis and deposition. The deposition of ISOPN, which involves gas–particle phase partition and subsequent hydrolysis (Jacobs et al., 2014), is not considered in the MXLCH. The lack of deposition process, however, could be partly compensated for by the fast photolysis rate of ISOPN in the model, which partly explains the agreement between the observation and the model output on ISOPN.

The reduced scheme overestimates formaldehyde (HCHO) concentration by 37 % at 10:00 CST. The difference between the two diminishes towards the late afternoon. The HCHO mixing ratio from the complex scheme output generally agrees with the observations throughout the simulation time period.

MXLCH reproduces the evolution of major chemical species within the CBL reasonably well, which provides confidence to carry out further analysis on the individual processes controlling the evolution of those compounds in the CBL. In Sect. 6.3 we discuss the influence of boundary layer dynamics and photochemistry on the evolution of O_3 and isoprene. In Sect. 6.4 we focus on interpretation of the isoprene photochemistry under different NO : HO_2 ratios.

6.3 Budget analysis of ozone and isoprene

Based on the output from the complex scheme, we applied a bulk budget analysis of O_3 and isoprene to differentiate between the impact of emission/deposition, entrainment, and chemical production/loss yields:

$$\frac{\partial \langle S \rangle}{\partial t} = \underbrace{\overbrace{\frac{F_S}{h}\sin\left(\frac{\pi t}{t_d}\right)}^{\text{Emission}} - \overbrace{\frac{V_d\langle S\rangle}{h}}^{\text{Deposition}} + \overbrace{\frac{w_e \Delta S}{h}}^{\text{Entrainment}}}_{\text{dynamics}} + \underbrace{\sum_i k_i \langle P1\rangle\langle P2\rangle - \sum_j k_j \langle S\rangle\langle \mathrm{Ox}_j\rangle - J\langle S\rangle}_{\text{chemistry}}, \quad (1)$$

where $\langle S \rangle$ is the mixed-layer mixing ratio of chemical species S (ppbv), h is the BLH (m), t is time (s), F_S is the maximum flux of S (ppbv m s^{-1}), t_d is the time length during which the heat flux is positive (s), V_d is the deposition velocity (cm s^{-1}), w_e is the entrainment velocity (m s^{-1}), k is the reaction rate coefficient (cm^3 molec.$^{-1}$ s^{-1}), $\langle P1 \rangle$ and $\langle P2 \rangle$ are the mixing ratio of the parent species (ppbv), $\langle \mathrm{Ox} \rangle$ is the mixed-layer mixing ratio of oxidants (ppbv), and J is photolysis rate coefficient (s^{-1}).

The total tendency of isoprene is largely controlled by emission and chemical loss. The emission tendency peaks at 08:50 CST, while the isoprene flux data peaks at 12:00 CST (Fig. S5). This difference is caused by the BLH evolution (Eq. 1). The chemical loss of isoprene is dominated by OH oxidation, with a small fraction (6 % of OH pathway) contributed by ozonolysis. As a result, the chemical tendency closely follows the variation in OH radicals, reaching a minimum during noontime. Since there is no chemical production of isoprene inside the CBL, chemistry acts as an isoprene loss throughout the whole model run. Entrainment acts as a dilution effect for isoprene since there is no isoprene in the FT; the minimum value in the entrainment tendency of isoprene at 09:00 CST therefore results from the rapid CBL growth and relatively shallow boundary layer (Fig. 4c) during this time period. During the early morning (06:00–10:00 CST), the total tendency of isoprene remains positive, reaching a peak value of 1.5 ppbv h^{-1} at 07:50 CST, which is caused by

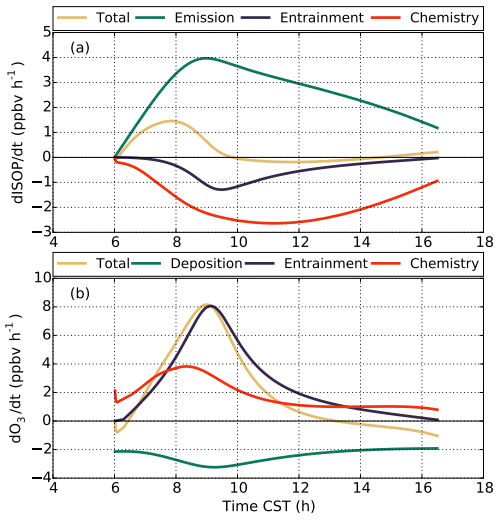

Figure 6. Contribution of dynamics and chemistry to the budgets of **(a)** isoprene and **(b)** ozone.

a combination of (1) increase in biogenic emission from forest canopy with an increase in ambient temperature and PAR (Guenther et al., 1995), (2) the relatively shallow boundary layer, and (3) the chemical loss due to OH oxidation is still low due to the low OH production inside the CBL. As a result, the emission term dominates the total tendency during this time period. During 10:00–15:00 CST, the total tendency is mainly controlled by the chemical loss. The high OH concentration induces a fast chemical loss rate of isoprene (with a maximum of $-2.6\,\mathrm{ppbv\,h^{-1}}$), bringing the total tendency to below zero during this time period.

Different from isoprene, entrainment primarily controls the total tendency of O_3 (Fig. 6b). The entrainment tendency is affected by entrainment velocity, mixing ratio difference between the FT and CBL, and the BLH (Eq. 1). During the early period of the simulation (at 06:00 CST), the entrainment tendency of O_3 experiences a rapid increase and reaches a peak value at 09:00 CST. This is caused by the interplay of (1) rapid growth of the BLH during the morning transition, (2) a large O_3 jump across the morning inversion layer (Table 3), and (3) a shallow BLH (Fig. 4c). After this time, the O_3 entrainment tendency decreases due to the decrease in entrainment velocity, reduced O_3 jump at the inversion layer, and the increase in the BLH. The second most important term controlling O_3 concentrations in the CBL is chemical production and loss, which is mainly controlled by the photolysis of O_3–NO_x system. The early morning peak value (at 08:30 CST) is due to the low photolysis rate caused by the large solar zenith angle. During noontime, increased O_3 photolysis induces a decrease in the chemical tendency, although the net value is still positive. The surface deposition tendency of O_3 is of comparable magnitude as the chemical tendency. The total O_3 tendency remains positive during 07:00–13:00 CST, reaching a peak value at 09:00 CST.

6.4 Photochemistry under different NO : HO_2

In Sect. 6.2, the model results show a wide range NO and HO_2 mixing ratios across the diurnal cycle (Fig. 5), which have varied impacts on the photochemistry inside the CBL. The term "low NO_x" can introduce ambiguity when interpreting ISOPOO chemistry (Liu et al., 2013). The definition for the threshold of "low NO_x" is usually arbitrarily based on either instrument performance or other standards during different laboratory or field experiments. For example, NO mixing ratios below 50 pptv (Lelieveld et al., 2008), 150 pptv (Xie et al., 2013), and 200 pptv (Lu et al., 2012) have all been used to indicate "low-NO_x" conditions. It has been suggested that "NO-dominant" or "HO_2-dominant" should be used instead when applying laboratory conditions to the atmospheric conditions (Liu et al., 2013; Wennberg, 2013). Here we use the ratio of NO to HO_2 (NO : HO_2, both in units of ppbv) to indicate the anthropogenic influence on ambient air composition and analyze the fate of isoprene and its photooxidization products under periods with different NO : HO_2 ratios. During the model simulation period (06:00–16:30 CST), NO and HO_2 concentrations vary in the range of 0.028–0.28 ppbv and 0.0018–0.030 ppbv, respectively (Fig. 8). The resulting NO : HO_2 ratio ranges from NO-dominant (NO : $HO_2 = 163$) to NO-HO_2-balanced (NO : $HO_2 = 1$) air conditions. Reaction with OH radicals is the major sink of isoprene due to its fast reaction rate with OH radicals under the observed meteorological conditions ($k_{C_5H_8+OH} = 1.0 \times 10^{-10}\,\mathrm{cm^3\,molec.^{-1}\,s^{-1}}$). Once emitted into the CBL, isoprene is rapidly oxidized through OH radical addition and subsequent reaction with O_2, producing a series of isomeric hydroxyl-substituted alkyl peroxyl radicals ($HOC_5H_8OO^{\bullet}$; ISOPOO). ISOPOO radicals go through several different pathways, including reactions with NO, HO_2, and RO_2, as well as isomerization (Table S3). The branching ratio of each pathway is strongly affected by NO and HO_2 mixing ratios.

The contribution from each reaction pathway listed above is plotted as a function of NO : HO_2, and the results are shown in Fig. 7. The NO pathway represents the major sink of ISOPOO radicals (> 85 %) under a wide range of NO : HO_2 (20–163). After NO : HO_2 falls below 20, the contribution from HO_2 pathway increases dramatically and reaches 54 % at NO : $HO_2 = 1$, while NO, isomerization, and the $CH_3(O)OO^{\cdot}$ pathway constitute 31, 11, and 3 %, respectively. For the RO_2 pathway, the $CH_3(O)OO^{\bullet}$ radical is the dominant candidate, and yet its contribution is negligible compared to the other reaction pathways throughout the whole NO : HO_2 range. The share of the NO pathway reaches 93 % under large NO : HO_2, while HO_2 and isomerization each contributes 3 and 4 %, respectively. With a box model simulation using MCM v3.2 constrained by chamber experiments, Liu et al. (2013) calculated the contributions from NO, HO_2, and isomerization pathways to be 93, 6, and 0.9 % under NO : $HO_2 = 32$. These results generally agree with this

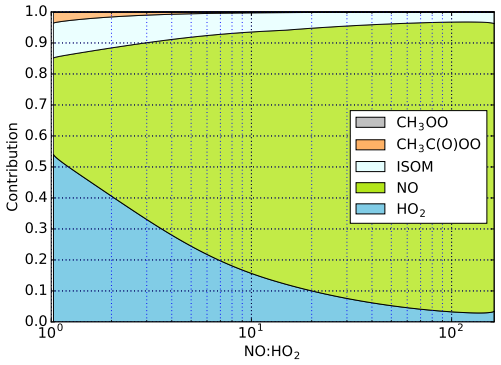

Figure 7. Relative contributions of different reaction pathways to the fate of ISOPOO radicals under different $NO:HO_2$. ISOM indicates isomerization. Data are from the MXLCH complex scheme with $F_{NO_x} = \pm 30\,\text{pptv}\,\text{m}\,\text{s}^{-1}$ and $\text{Yield}_{ISOPN} = 6\,\%$.

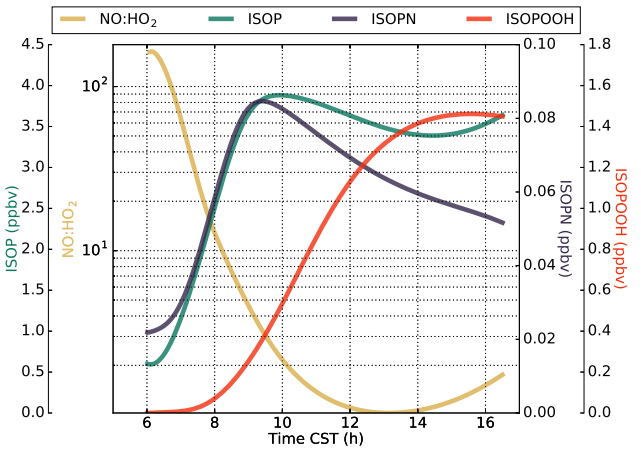

Figure 8. Diurnal evolutions of isoprene nitrates (ISOPN), isoprene hydroxy hydroperoxides (ISOPOOH), isoprene (ISOP), and $NO:HO_2$ from the MXLCH complex scheme with $F_{NO_x} = \pm 30\,\text{pptv}\,\text{m}\,\text{s}^{-1}$ and $\text{Yield}_{ISOPN} = 6\,\%$.

study under the same $NO:HO_2$ value (88, 7, and 4 %, respectively). Both studies used the isomerization rate coefficient from Crounse et al. (2011). The low end of $NO:HO_2$ in Liu et al. (2013) (< 1) is out of the range of our model results.

ISOPN and ISOPOOH are the two tracers of isoprene photooxidation under NO- and HO_2-dominant conditions. The diurnal evolution of these two compounds together with $NO:HO_2$ and isoprene mixing ratios is shown in Fig. 8. The rapid increase in ISOPN mixing ratios ($0.032\,\text{ppbv}\,\text{h}^{-1}$) during 06:00–09:00 CST coincides with the NO peak during the same time period (0.10–0.28 ppbv, Fig. 5b). The $NO:HO_2$ ratio spans a large range (5–160) during this time period, which corresponds to a 66–93 % sink of ISOPOO radicals through the NO pathway (Fig. 7). Under this NO-dominant air condition, the ISOPN mixing ratios are mainly constrained by the availability of isoprene during this time period, which is reflected by the high correlation between these two species. After 09:00 CST, the $NO:HO_2$ falls below 5 and stays at ~ 1 during 12:00–16:00 CST. The ISOPN mixing ratios start to decrease even though the isoprene (3–4 ppbv) is still abundant in the CBL. This is due to the shift from NO-dominant to NO-HO_2-balanced conditions, and ISOPN production becomes constrained by NO availability. Meanwhile, ISOPN is relatively short lived (chemical lifetime of 2 h) under the OH radical concentration of $\sim 1.5 \times 10^6$ molec. cm^{-3}.

The mixing ratio of ISOPOOH shows reversed correlation with $NO:HO_2$: ISOPOOH starts to rise after 07:00 CST and reaches 1.5 ppbv at 16:00 CST. The higher mixing ratio of ISOPOOH during the end of the model simulation is a result of (1) sufficient isoprene and HO_2 radicals and (2) the longer chemical life time of ISOPOOH (5 h) due to reduced OH radicals in the CBL. The peak value of the ISOPOOH mixing ratio predicted by MXLCH (1.5 ppbv) is significantly higher than ground-based observations at the SEARCH site (0.40 ppbv, measured on 8 June 2013) (Nguyen et al., 2015). The dry deposition velocity of ISOPOOH in MXLCH is set to $2.5\,\text{cm}\,\text{s}^{-1}$, which is adopted from the same ground-based observation at the SEARCH site (Nguyen et al., 2015). One possible explanation of the large discrepancy between model output and observation is some missing chemical sink paths of ISOPOOH in the complex scheme. Another explanation, although less possible, is the partitioning of ISOPOOH to the aerosol phase due to its lower vapor pressure and potentially high condensed-phase reactivity (Rivera-Rios et al., 2014). For simplicity, aerosol–gas-phase chemistry is not implemented in this study. Future work should incorporate an aerosol phase module into MXLCH. Despite the higher ISOPOOH mixing ratios from MXLCH, the averaged value of ISOPOOH/ISOPN values from MXLCH (13; both species are in units of ppbv) is within the range of the GEOS-Chem model outputs for time period of August 2013 over the southeastern US (5–15) (Kim et al., 2015).

7 Conclusions

The WASP system enabled us to quantify the vertical profiles of VOC species inside the CBL at high temporal (hourly) resolution. Before sunrise, isoprene and MVK + MACR exhibit lower mixing ratios (< 1.00 ppbv) within and above the CBL. This is due to the absence of solar radiation, which drives biological isoprene production, and convective turbulent mixing. Monoterpenes, on the other hand, have a large contrast in mixing ratios within and above the CBL in early morning. This is largely attributed to nighttime emissions and a lack of vertical turbulent mixing, trapping the monoterpenes within the nocturnal boundary layer's limited depth. During sunlit noontime, observed vertical profiles of isoprene and monoterpenes reveal a vertical gradient within the CBL, with higher mixing ratios near the forest canopy and low values towards the top of the CBL.

The MXLCH model generally reproduces the boundary layer's diurnal evolution (e.g., BLH growth, potential temperature, and specific humidity). Accurate modeling of BLH is essential for investigating trace-gas photochemistry in that the FT–CBL exchange plays an important role in regulating the vertical distribution and evolution of trace-gas species in the CBL through entrainment.

Budget analyses show that the diurnal evolution of O_3 is mainly controlled by entrainment. Isoprene photochemistry is strongly influenced by $NO : HO_2$ values. This is reflected through the fate of ISOPOO radicals, which shift from a NO-dominant pathway (with a contribution of 93 %) to a NO-HO_2-balanced pathway (with a contribution of 54 %) from early morning ($NO : HO_2 = 163$) to noontime ($NO : HO_2 = 1$). As a result, ISOPN and ISOPOOH show peaks during 09:00 CST and 16:00 CST, respectively. ISOPN production is constrained by isoprene before 09:00 CST. The mixing ratio of ISOPN decreases after 09:00 CST due to its short lifetime (2 h) and limited NO availability. ISOPOOH is inversely correlated with $NO : HO_2$. Model outputs significantly overestimate ISOPOOH mixing ratios in the late afternoon when compared with ground-based observation, with implications for missing sinks of ISOPOOH.

8 Data availability

The observational data used in this paper are available at: http://www.esrl.noaa.gov/csd/projects/senex/ (NOAA, 2016).

The Supplement related to this article is available online at doi:10.5194/acp-16-7725-2016-supplement.

Acknowledgements. We thank the organizers of the SAS and FIXCIT study. We especially thank A. Turnipseed for providing VOC standard gas during the campaign and B. Hansen from Vaiden Field Airport for logistics. We would like to acknowledge operational, technical, and scientific support provided by NCAR's Earth Observing Laboratory, sponsored by the National Science Foundation. We thank the GEOS-Chem and MOZART model community. M. Dorris helped with the formaldehyde measurement. This study is supported by US Environmental Protection Agency (EPA) STAR program (grant R835407), the National Science Foundation (NSF, grant AGS-1628530), and UltraPure Air, LLC. E. G. Patton was supported by NCAR's "Bio-hydro-atmosphere interactions of Energy, Aerosols, Carbon, H_2O, Organics and Nitrogen" (BEACHON) project.

Edited by: R. McLaren

References

Cappellin, L., Karl, T., Probst, M., Ismailova, O., Winkler, P. M., Soukoulis, C., Aprea, E., Mark, T. D., Gasperi, F., and Biasioli, F.: On Quantitative Determination of Volatile Organic Compound Concentrations Using Proton Transfer Reaction Time-of-Flight Mass Spectrometry, Environ. Sci. Technol., 46, 2283–2290, 2012.

Crounse, J. D., Paulot, F., Kjaergaard, H. G., and Wennberg, P. O.: Peroxy radical isomerization in the oxidation of isoprene, Phys. Chem. Chem. Phys., 13, 13607–13613, doi:10.1039/C1cp21330j, 2011.

de Arellano, J. V. G., Patton, E. G., Karl, T., van den Dries, K., Barth, M. C., and Orlando, J. J.: The role of boundary layer dynamics on the diurnal evolution of isoprene and the hydroxyl radical over tropical forests, J. Geophys. Res.-Atmos., 116, D07304, doi:10.1029/2010JD014857, 2011.

de Arellano, J. V. G., van Heerwaarden, C. C., van Stratum, B. J. H., and van den Dries, K.: Atmospheric Boundary Layer: Integrating air chemistry and land interactions, Cambridge University Press, 2015.

Emmons, L. K., Walters, S., Hess, P. G., Lamarque, J.-F., Pfister, G. G., Fillmore, D., Granier, C., Guenther, A., Kinnison, D., Laepple, T., Orlando, J., Tie, X., Tyndall, G., Wiedinmyer, C., Baughcum, S. L., and Kloster, S.: Description and evaluation of the Model for Ozone and Related chemical Tracers, version 4 (MOZART-4), Geosci. Model Dev., 3, 43–67, doi:10.5194/gmd-3-43-2010, 2010.

Gao, W., Wesely, M. L., and Doskey, P. V.: Numerical Modeling of the Turbulent-Diffusion and Chemistry of NO_x, O_3, Isoprene, and Other Reactive Trace Gases in and above a Forest Canopy, J. Geophys. Res.-Atmos., 98, 18339–18353, 1993.

Geddes, J. A. and Murphy, J. G.: Observations of reactive nitrogen oxide fluxes by eddy covariance above two midlatitude North American mixed hardwood forests, Atmos. Chem. Phys., 14, 2939–2957, doi:10.5194/acp-14-2939-2014, 2014.

Graus, M., Muller, M., and Hansel, A.: High Resolution PTR-TOF: Quantification and Formula Confirmation of VOC in Real Time, J. Am. Soc. Mass. Spectr., 21, 1037–1044, 2010.

Guenther, A., Hewitt, C. N., Erickson, D., Fall, R., Geron, C., Graedel, T., Harley, P., Klinger, L., Lerdau, M., Mckay, W. A., Pierce, T., Scholes, B., Steinbrecher, R., Tallamraju, R., Taylor, J., and Zimmerman, P.: A Global-Model of Natural Volatile Organic-Compound Emissions, J. Geophys. Res.-Atmos., 100, 8873–8892, 1995.

Guenther, A. B., Monson, R. K., and Fall, R.: Isoprene and Monoterpene Emission Rate Variability – Observations with Eucalyptus and Emission Rate Algorithm Development, J. Geophys. Res.-Atmos., 96, 10799–10808, 1991.

Hidy, G. M., Blanchard, C. L., Baumann, K., Edgerton, E., Tanenbaum, S., Shaw, S., Knipping, E., Tombach, I., Jansen, J., and Walters, J.: Chemical climatology of the southeastern United States, 1999–2013, Atmos. Chem. Phys., 14, 11893–11914, doi:10.5194/acp-14-11893-2014, 2014.

Hofzumahaus, A., Rohrer, F., Lu, K. D., Bohn, B., Brauers, T., Chang, C. C., Fuchs, H., Holland, F., Kita, K., Kondo, Y., Li, X., Lou, S. R., Shao, M., Zeng, L. M., Wahner, A., and Zhang, Y. H.: Amplified Trace Gas Removal in the Troposphere, Science, 324, 1702–1704, 2009.

Jacobs, M. I., Burke, W. J., and Elrod, M. J.: Kinetics of the reactions of isoprene-derived hydroxynitrates: gas phase epoxide formation and solution phase hydrolysis, Atmos. Chem. Phys., 14, 8933–8946, doi:10.5194/acp-14-8933-2014, 2014.

Jordan, A., Haidacher, S., Hanel, G., Hartungen, E., Mark, L., Seehauser, H., Schottkowsky, R., Sulzer, P., and Mark, T. D.: A high resolution and high sensitivity proton-transfer-reaction time-of-flight mass spectrometer (PTR-TOF-MS), Int. J. Mass. Spectrom., 286, 122–128, 2009.

Karl, T., Guenther, A., Yokelson, R. J., Greenberg, J., Potosnak, M., Blake, D. R., and Artaxo, P.: The tropical forest and fire emissions experiment: Emission, chemistry, and transport of biogenic volatile organic compounds in the lower atmosphere over Amazonia, J. Geophys. Res.-Atmos., 112, D18302, doi:10.1029/2007JD008539, 2007.

Karl, T., Misztal, P. K., Jonsson, H. H., Shertz, S., Goldstein, A. H., and Guenther, A. B.: Airborne Flux Measurements of BVOCs above Californian Oak Forests: Experimental Investigation of Surface and Entrainment Fluxes, OH Densities, and Damkohler Numbers, J. Atmos. Sci., 70, 3277–3287, doi:10.1175/Jas-D-13-054.1, 2013.

Kim, P. S., Jacob, D. J., Fisher, J. A., Travis, K., Yu, K., Zhu, L., Yantosca, R. M., Sulprizio, M. P., Jimenez, J. L., Campuzano-Jost, P., Froyd, K. D., Liao, J., Hair, J. W., Fenn, M. A., Butler, C. F., Wagner, N. L., Gordon, T. D., Welti, A., Wennberg, P. O., Crounse, J. D., St. Clair, J. M., Teng, A. P., Millet, D. B., Schwarz, J. P., Markovic, M. Z., and Perring, A. E.: Sources, seasonality, and trends of southeast US aerosol: an integrated analysis of surface, aircraft, and satellite observations with the GEOS-Chem chemical transport model, Atmos. Chem. Phys., 15, 10411–10433, doi:10.5194/acp-15-10411-2015, 2015.

Kim, S., Karl, T., Guenther, A., Tyndall, G., Orlando, J., Harley, P., Rasmussen, R., and Apel, E.: Emissions and ambient distributions of Biogenic Volatile Organic Compounds (BVOC) in a ponderosa pine ecosystem: interpretation of PTR-MS mass spectra, Atmos. Chem. Phys., 10, 1759–1771, doi:10.5194/acp-10-1759-2010, 2010.

Kristensen, L., Lenschow, D. H., Gurarie, D., and Jensen, N. O.: A Simple Model for the Vertical Transport of Reactive Species in the Convective Atmospheric Boundary Layer, Bound.-Lay. Meteorol., 134, 195–221, doi:10.1007/s10546-009-9443-x, 2010.

Lee, L., Teng, A. P., Wennberg, P. O., Crounse, J. D., and Cohen, R. C.: On Rates and Mechanisms of OH and O_3 Reactions with Isoprene-Derived Hydroxy Nitrates, J. Phys. Chem. A, 118, 1622–1637, doi:10.1021/jp4107603, 2014.

Lelieveld, J., Butler, T. M., Crowley, J. N., Dillon, T. J., Fischer, H., Ganzeveld, L., Harder, H., Lawrence, M. G., Martinez, M., Taraborrelli, D., and Williams, J.: Atmospheric oxidation capacity sustained by a tropical forest, Nature, 452, 737–740, 2008.

Liu, Y. J., Herdlinger-Blatt, I., McKinney, K. A., and Martin, S. T.: Production of methyl vinyl ketone and methacrolein via the hydroperoxyl pathway of isoprene oxidation, Atmos. Chem. Phys., 13, 5715–5730, doi:10.5194/acp-13-5715-2013, 2013.

Lu, K. D., Rohrer, F., Holland, F., Fuchs, H., Bohn, B., Brauers, T., Chang, C. C., Häseler, R., Hu, M., Kita, K., Kondo, Y., Li, X., Lou, S. R., Nehr, S., Shao, M., Zeng, L. M., Wahner, A., Zhang, Y. H., and Hofzumahaus, A.: Observation and modelling of OH and HO_2 concentrations in the Pearl River Delta 2006: a missing OH source in a VOC rich atmosphere, Atmos. Chem. Phys., 12, 1541–1569, doi:10.5194/acp-12-1541-2012, 2012.

Mak, J. E., Su, L., Guenther, A., and Karl, T.: A novel Whole Air Sample Profiler (WASP) for the quantification of volatile organic compounds in the boundary layer, Atmos. Meas. Tech., 6, 2703–2712, doi:10.5194/amt-6-2703-2013, 2013.

Mao, J. Q., Paulot, F., Jacob, D. J., Cohen, R. C., Crounse, J. D., Wennberg, P. O., Keller, C. A., Hudman, R. C., Barkley, M. P., and Horowitz, L. W.: Ozone and organic nitrates over the eastern United States: Sensitivity to isoprene chemistry, J. Geophys. Res.-Atmos., 118, 11256–11268, doi:10.1002/jgrd.50817, 2013.

Min, K.-E., Pusede, S. E., Browne, E. C., LaFranchi, B. W., and Cohen, R. C.: Eddy covariance fluxes and vertical concentration gradient measurements of NO and NO_2 over a ponderosa pine ecosystem: observational evidence for within-canopy chemical removal of NO_x, Atmos. Chem. Phys., 14, 5495–5512, doi:10.5194/acp-14-5495-2014, 2014.

Muller, J. F., Peeters, J., and Stavrakou, T.: Fast photolysis of carbonyl nitrates from isoprene, Atmos. Chem. Phys., 14, 2497–2508, doi:10.5194/acp-14-2497-2014, 2014.

Nguyen, T. B., Crounse, J. D., Teng, A. P., Clair, J. M. S., Paulot, F., Wolfe, G. M., and Wennberg, P. O.: Rapid deposition of oxidized biogenic compounds to a temperate forest, P. Natl. Acad. Sci. USA, 112, E392–E401, doi:10.1073/pnas.1418702112, 2015.

NOAA: SENEX 2013, available at: http://www.esrl.noaa.gov/csd/projects/senex/, last access: 21 June 2016.

Orlando, J. J. and Tyndall, G. S.: Laboratory studies of organic peroxy radical chemistry: an overview with emphasis on recent issues of atmospheric significance, Chem. Soc. Rev., 41, 6294–6317, 2012.

Ouwersloot, H. G., Vilà-Guerau de Arellano, J., van Heerwaarden, C. C., Ganzeveld, L. N., Krol, M. C., and Lelieveld, J.: On the segregation of chemical species in a clear boundary layer over heterogeneous land surfaces, Atmos. Chem. Phys., 11, 10681–10704, doi:10.5194/acp-11-10681-2011, 2011.

Park, J.-H., Goldstein, A. H., Timkovsky, J., Fares, S., Weber, R., Karlik, J., and Holzinger, R.: Eddy covariance emission and deposition flux measurements using proton transfer reaction – time of flight – mass spectrometry (PTR-TOF-MS): comparison with PTR-MS measured vertical gradients and fluxes, Atmos. Chem. Phys., 13, 1439–1456, doi:10.5194/acp-13-1439-2013, 2013.

Patton, E. G., Davis, K. J., Barth, M. C., and Sullivan, P. P.: Decaying scalars emitted by a forest canopy: A numerical study, Bound.-Lay. Meteorol., 100, 91–129, 2001.

Paulot, F., Crounse, J. D., Kjaergaard, H. G., Kurten, A., St Clair, J. M., Seinfeld, J. H., and Wennberg, P. O.: Unexpected Epoxide Formation in the Gas-Phase Photooxidation of Isoprene, Science, 325, 730–733, 2009.

Peeters, J., Nguyen, T. L., and Vereecken, L.: HO_x radical regeneration in the oxidation of isoprene, Phys. Chem. Chem. Phys., 11, 5935–5939, 2009.

Peeters, J. and Muller, J. F.: HO_x radical regeneration in isoprene oxidation via peroxy radical isomerisations. II: experimental evidence and global impact, Phys. Chem. Chem. Phys., 12, 14227–14235, 2010.

Rivera-Rios, J. C., Nguyen, T. B., Crounse, J. D., Jud, W., St Clair, J. M., Mikoviny, T., Gilman, J. B., Lerner, B. M., Kaiser, J. B., de Gouw, J., Wisthaler, A., Hansel, A., Wennberg, P. O., Seinfeld, J. H., and Keutsch, F. N.: Conversion of hydroperoxides

to carbonyls in field and laboratory instrumentation: Observational bias in diagnosing pristine versus anthropogenically controlled atmospheric chemistry, Geophys. Res. Lett., 41, 8645–8651, doi:10.1002/2014gl061919, 2014.

Shirley, T. R., Brune, W. H., Ren, X., Mao, J., Lesher, R., Cardenas, B., Volkamer, R., Molina, L. T., Molina, M. J., Lamb, B., Velasco, E., Jobson, T., and Alexander, M.: Atmospheric oxidation in the Mexico City Metropolitan Area (MCMA) during April 2003, Atmos. Chem. Phys., 6, 2753–2765, doi:10.5194/acp-6-2753-2006, 2006.

Thornton, F. C., Pier, P. A., and Valente, R. J.: NO emissions from soils in the southeastern United States, J. Geophys. Res.-Atmos., 102, 21189–21195, doi:10.1029/97jd01567, 1997.

van Stratum, B. J. H., Vilà-Guerau de Arellano, J., Ouwersloot, H. G., van den Dries, K., van Laar, T. W., Martinez, M., Lelieveld, J., Diesch, J.-M., Drewnick, F., Fischer, H., Hosaynali Beygi, Z., Harder, H., Regelin, E., Sinha, V., Adame, J. A., Sörgel, M., Sander, R., Bozem, H., Song, W., Williams, J., and Yassaa, N.: Case study of the diurnal variability of chemically active species with respect to boundary layer dynamics during DOMINO, Atmos. Chem. Phys., 12, 5329–5341, doi:10.5194/acp-12-5329-2012, 2012.

Vilà-Guerau de Arellano, J.: MiXed Layer CHemistry (MXLCH) model, Meteorology and Air Quality Section, Wageningen University and Research Centre, Wageningen, the Netherlands, available at: https://github.com/classmodel/mxlch, last access: 21 June 2016.

Wennberg, P. O.: Let's abandon the "high NO_x" and "low NO_x" terminology, IGAC News, 3–4, 2013.

Whalley, L. K., Furneaux, K. L., Goddard, A., Lee, J. D., Mahajan, A., Oetjen, H., Read, K. A., Kaaden, N., Carpenter, L. J., Lewis, A. C., Plane, J. M. C., Saltzman, E. S., Wiedensohler, A., and Heard, D. E.: The chemistry of OH and HO_2 radicals in the boundary layer over the tropical Atlantic Ocean, Atmos. Chem. Phys., 10, 1555–1576, doi:10.5194/acp-10-1555-2010, 2010.

Whalley, L. K., Edwards, P. M., Furneaux, K. L., Goddard, A., Ingham, T., Evans, M. J., Stone, D., Hopkins, J. R., Jones, C. E., Karunaharan, A., Lee, J. D., Lewis, A. C., Monks, P. S., Moller, S. J., and Heard, D. E.: Quantifying the magnitude of a missing hydroxyl radical source in a tropical rainforest, Atmos. Chem. Phys., 11, 7223–7233, doi:10.5194/acp-11-7223-2011, 2011.

Xie, Y., Paulot, F., Carter, W. P. L., Nolte, C. G., Luecken, D. J., Hutzell, W. T., Wennberg, P. O., Cohen, R. C., and Pinder, R. W.: Understanding the impact of recent advances in isoprene photooxidation on simulations of regional air quality, Atmos. Chem. Phys., 13, 8439–8455, doi:10.5194/acp-13-8439-2013, 2013.

Xiong, F., McAvey, K. M., Pratt, K. A., Groff, C. J., Hostetler, M. A., Lipton, M. A., Starn, T. K., Seeley, J. V., Bertman, S. B., Teng, A. P., Crounse, J. D., Nguyen, T. B., Wennberg, P. O., Misztal, P. K., Goldstein, A. H., Guenther, A. B., Koss, A. R., Olson, K. F., de Gouw, J. A., Baumann, K., Edgerton, E. S., Feiner, P. A., Zhang, L., Miller, D. O., Brune, W. H., and Shepson, P. B.: Observation of isoprene hydroxynitrates in the southeastern United States and implications for the fate of NO_x, Atmos. Chem. Phys., 15, 11257–11272, doi:10.5194/acp-15-11257-2015, 2015.